International Journal of
Molecular Sciences

Article

Ab Initio Study of Formation Mechanisms and Thermochemical Properties of Reactive Oxygen Species (ROS) in Photocatalytic Processes

Silvia González and Ximena Jaramillo-Fierro *

Departamento de Química, Facultad de Ciencias Exactas y Naturales, Universidad Técnica Particular de Loja, San Cayetano Alto, Loja 1101608, Ecuador; sgonzalez@utpl.edu.ec
* Correspondence: xvjaramillo@utpl.edu.ec; Tel.: +593-7-3701444

Abstract

This study explores the thermochemical properties and formation mechanisms of reactive oxygen species (ROS) relevant to photocatalytic processes, aiming to clarify their molecular characteristics and reaction dynamics. The research focuses on key ROS, including the superoxide anion radical ($^{\bullet}O_2^{-}$), hydrogen peroxide (H_2O_2), singlet oxygen ($^1O_2$), and hydroxyl radical ($^{\bullet}OH$), employing Møller–Plesset second-order perturbation theory (MP2)-level quantum chemical calculations. Solvent effects were modeled using water to simulate conditions commonly found in photocatalytic environments. The computed energetic profiles and stabilities of the ROS offer insights into their relative reactivities and possible interconversion pathways. These findings enhance the understanding of how ROS behave under photocatalytic conditions, with implications for their role in degradation mechanisms and redox cycles. Overall, the results support the development and optimization of photocatalytic technologies for environmental applications, including pollutant degradation and disinfection of water and air.

Keywords: reactive oxygen species; photocatalysis; quantum chemical calculations; MP2 method; thermochemical properties

Academic Editor: María Teresa Colomer

Received: 3 August 2025
Revised: 7 September 2025
Accepted: 12 September 2025
Published: 15 September 2025

Citation: González, S.; Jaramillo-Fierro, X. Ab Initio Study of Formation Mechanisms and Thermochemical Properties of Reactive Oxygen Species (ROS) in Photocatalytic Processes. *Int. J. Mol. Sci.* **2025**, *26*, 8989. https://doi.org/10.3390/ijms26188989

1. Introduction

Photocatalysis utilizes light energy to drive chemical reactions by generating electron/hole pairs (e−/h+) within a semiconductor catalyst [1]. These photogenerated charge carriers interact with oxygen and water molecules, leading to the formation of reactive oxygen species (ROS) such as superoxide anion radical ($^{\bullet}O_2^{-}$), hydrogen peroxide (H_2O_2), singlet oxygen ($^1O_2$), and hydroxyl radical ($^{\bullet}OH$) [2–4]. These species exhibit distinct redox properties, enabling their participation in oxidation-reduction reactions relevant to environmental and biological processes [5–10]. However, their reactivity and stability strongly depend on external factors, including oxygen concentration, pH and the presence of catalytic sites [11,12]. Recent studies have shown that structural modifications of photocatalysts, such as incorporating metal-semiconductor heterojunctions, can optimize ROS production and regulation, favoring specific reaction pathways and improving efficiency in contaminant degradation [13,14].

ROS formation in photocatalysis primarily occurs through electron transfer reactions and energy transfer mechanisms [15]. Superoxide anion ($^{\bullet}O_2^{-}$) is typically formed by the single-electron reduction in molecular oxygen (O_2) facilitated by conduction band electrons from the photocatalyst [16]. In contrast, singlet oxygen ($^1O_2$) arises from an energy transfer process, where an excited photocatalyst transfers energy to molecular oxygen, altering Its spin state to form a highly reactive species [17]. Hydrogen peroxide (H_2O_2) can be generated either by the interaction of the superoxide radical ($^\bullet O_2{}^-$) with protons and electrons or through the recombination of hydroxyl radical ($^\bullet OH$). Among these species, hydroxyl radical ($^\bullet OH$) is the most reactive, capable of oxidizing almost any organic or inorganic molecule. Its formation is often associated with water oxidation by valence band holes or via interactions with pre-existing ROS, such as superoxide anions and hydrogen peroxide [18,19]. In heterogeneous photocatalysis, pH-dependent speciation and redox potentials govern ROS interconversion (e.g., $HO_2\bullet/O_2\bullet^-$ equilibrium; Nernstian shifts), and interfacial adsorption/charge can dominate the apparent reactivity (e.g., $^\bullet OH$ adsorbed as trapped holes; peroxo-like bridged surface species/H_2O_2) [20]. These experimentally established features provide the context in which we interpret the thermodynamic maps presented in this study.

The reactivity of ROS makes them critical in natural and engineered systems. In the environment, ROS are key players in biogeochemical cycles, affecting pollutant degradation and redox equilibria in water and atmospheric systems. Recent studies highlight how oxygen concentration and transition metals influence ROS formation, particularly in aquatic and atmospheric environments [21].

The generation and transformation of ROS in the environment play a fundamental role in biogeochemical cycles and the natural degradation of contaminants [22]. Recent studies have highlighted the influence of environmental factors such as oxygen concentration and the presence of transition metals on ROS formation in aquatic and atmospheric media [23]. Additionally, the development of high-entropy oxides has been identified as a promising strategy for the efficient activation of molecular oxygen in sustainable photocatalytic processes, promoting selective ROS generation and reducing the need for expensive catalysts [24]. Beyond their application in decontamination processes, ROS have found utility in biomedical fields, particularly in therapies based on the selective cytotoxicity of these species. Nanoplatforms that generate ROS have been reported for cancer treatment, where these species induce apoptosis through controlled oxidative stress mechanisms [25].

Reactive oxygen species (ROS) are important intermediates in oxidation and reduction reactions that occur near the surface of photocatalysts such as titanium dioxide (TiO_2) [26–28], zinc titanate ($ZnTiO_3$) [29], zinc oxide (ZnO) [30], and others. These processes include the oxidation of organics and reduction in inorganic molecules [31,32]. Thus, efficient generation of ROS is fundamental for optimizing the efficiency of photocatalytic processes [33,34]. The adsorption of molecules on the catalyst surface is not a prerequisite for efficient oxidation-reduction. In fact, the oxidation and reduction reactions that occur by photooxidation could occur in the bulk solution where ROS plays a key role. In this way, the contribution of ROS located on the surface of the catalyst is reduced [35]. Literature suggests that photocatalytic generation of ROS on TiO_2 surfaces predominantly occurs through reactions at the anionic bridge OH site and the cationic terminal OH site. At the anionic bridge OH site, a proposed mechanism involves nucleophilic oxidation of water, where a photoinduced hole targets the $O(^{2-})$ bridge, generating a hydroxyl radical ($^\bullet OH$). Conversely, at the cationic terminal OH site, where positively charged holes are unreactive, it is proposed that a photoinduced electron trapped at the TiO_2 surface reduces O_2, forming the superoxide anion radical ($^\bullet O_2{}^-$) [36].

Despite extensive interest in surface ROS reactions due to their diverse chemical applications, there remains a notable lack of detailed understanding regarding the thermochemical properties and generation pathways of several ROS, including the superoxide anion radical ($^\bullet O_2{}^-$), hydrogen peroxide (H_2O_2), singlet oxygen ($^1O_2$), and hydroxyl radical ($^{\bullet}$OH). The stability and generation pathways of reactive oxygen species (ROS) are influenced by their thermochemical properties, which can be difficult to determine by experimental methods due to their short half-lives and their tendency to rapidly transform into other species because of their high reactivity. In this way, computational methods are a valuable tool to evaluate the stability and formation mechanisms of these species, as well as their possible transformations in various processes [35].

Methods such as Density Functional Theory (DFT) and Møller–Plesset second-order perturbation theory (MP2) have been widely used to evaluate the stability and reactivity of those species and systems. Recent studies have proposed improvements in MP2 calculations for the prediction of weak interactions, providing a better approximation of experimentally observed phenomena [37]. Additionally, advanced techniques such as Laplace-transformed MP2 have optimized the simulation of periodic systems, allowing for more accurate assessments of photocatalytic materials [38]. MP2 calculations can elucidate the stability of ROS intermediates by determining their energetic profiles and relative stabilities compared to those of other species. Therefore, this MP2 study investigated the thermochemical properties and formation reactions of key ROS generated during photocatalytic processes: the superoxide anion radical ($^{\bullet}O_2^{-}$), hydrogen peroxide (H_2O_2), singlet oxygen ($^1O_2$), and hydroxyl radical ($^{\bullet}$OH). Understanding these properties and reactions can disclose potential pathways for ROS generation and control their reactivity.

Recent literature reviews highlight the importance of ROS generation and regulation in photocatalysis, not only for contaminant degradation but also for emerging applications in biomedicine and energy conversion. This study fits within this context, addressing the stability and reactivity of ROS through advanced computational methodologies and exploring their applicability in environmental remediation processes and sustainable energy production. The combination of experimental and theoretical strategies will help advance the understanding of these processes and the development of more efficient and sustainable technologies [22,25,37,38].

2. Results

2.1. O_2 Species

Table 1 summarizes the thermochemical and molecular properties of O_2(T), $^1O_2$(S), and $^{\bullet}O_2^{-}$(D). The units for Gibbs free energy (G°) and total energy (E°) are expressed in atomic units of energy (a.u.e) o hartrees (ha). Bond distances ($d_{O\text{-}O}$) are in Angstroms (Å); the dipole moment (μ), indicating directional charge distribution polarizations, is in Debyes; electronic spatial extent (R^2) in Angstroms squared (Å^2), and the vibrational frequency ($\nu_{O\text{-}O}$) is in inverse centimeters (cm^{-1}).

Table 1. Thermochemistry and calculated molecular properties of oxygen molecules. Between parenthesis, the multiplicity of each species is described (T = triplet, S = singlet and D = doublet). The ($^{\bullet}$) symbol indicates that the species is radical and the negative sign as super-index indicates that the species has negative charge.

Species	E° (Hartree)	G° (Hartree)	$d_{O\text{-}O}$ (Å)	$\nu_{O\text{-}O}$ (cm^{-1})	μ (Debye)	R^2 (Å^2)
O_2(T)	−150.04	−150.06	1.23	1423	0	12.43
$^1O_2$(S)	−149.99	−150.01	1.26	1216	0	12.75
$^{\bullet}O_2^{-}$(D)	−150.15	−150.17	1.37	1064	0	16.02

Formation Reactions of O_2 Species

The photogeneration of radical oxygen species, specifically singlet oxygen $^1O_2$(S) and the superoxide radical $^{\bullet}O_2^{-}$(D) from triplet oxygen O_2(T), the most abundant and stable form of oxygen, can follow two distinct pathways. The calculated reaction energy values for these pathways are presented in Table 2. Reaction (3) is the inverse of Reaction (2). Both are included because they illustrate the obtention of two different species, $^{\bullet}O_2^-$(D) and $^1O_2$(S), each of which participates in other reactions to obtain other ROS.

Table 2. Possible reactions between the three oxygen species. The energy difference between species in reactions is obtained from the difference between the sum of the energy of the reaction products and the sum of the energy of the reactants.

Reaction		ΔE (kJ mol^{-1}) *	ΔG (kJ mol^{-1})
$O_2(T) \rightarrow {}^1O_2(S)$	(1)	124	126
${}^1O_2(S) \rightarrow {}^{\bullet}O_2^-(D) + e^-$	(2)	−405	−407
${}^{\bullet}O_2^-(D) + h^+ \rightarrow {}^1O_2(S)$	(3)	405	407
$O_2(T) + e^- \rightarrow {}^{\bullet}O_2^-(D)$	(4)	−281	−281

* The energy difference between species in reactions is obtained from the difference between the sum of the total energy or free energy of the reaction products and the sum of the total energy or free energy of the reactants.

Figure 1 illustrates the calculated pathways for the formation of the $^{\bullet}O_2^-$(D) species. In this figure, blue arrows indicate the transformations between species. Singlet oxygen $^1O_2$(S) is represented with a pair of electrons in opposite directions, triplet oxygen O_2(T) with two unpaired electrons in the same direction, and doublet oxygen $^{\bullet}O_2^-$(D) is depicted with a black sphere, indicating its radical nature.

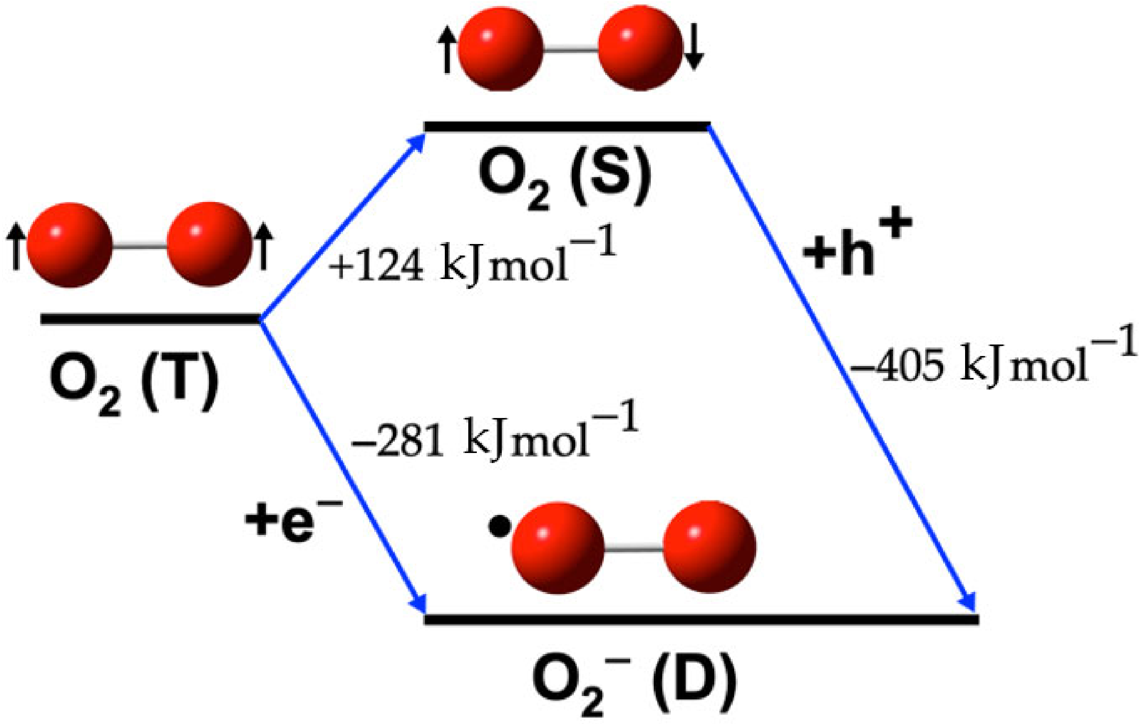

Figure 1. Calculated pathways for the formation of $^{\bullet}O_2^-$(D) species. The blue arrows indicate the transformations between species.

Several reactions involving ROS are initiated by the superoxide radical anion $^{\bullet}O_2^-$(D). This species exhibits high oxidative activity, although selective and medium-dependent. The combination of its redox couples and pH-dependent speciation ($HO_2\bullet/{}^{\bullet}O_2^-$ equilibrium) accounts for its reactivity toward suitable substrates; in particular, protonation ($pK_a \approx 4.8$) and $HO_2\bullet/{}^{\bullet}O_2^-$ disproportionation supports both the stronger oxidizing character at acidic pH and the marked pH dependence [39]. This behavior has been verified experimentally: (i) in the aerobic degradation of p-nitrophenol, EPR spin-trapping and quenching assays identify $^\bullet O_2^-$ as the key species with preferential attack at the nitro group, and (ii) in heterogeneous photocatalysis, measurable kinetics with phenols show Hammett-type substituent correlations for $^\bullet O_2^-$-mediated oxidation, evidencing effective yet selective reactivity [20,39,40]. Moreover, its longer lifetime in water relative to $^\bullet OH$ favors participation in multiple downstream pathways, including H_2O_2 formation via disproportionation, reinforcing its role as an active and versatile oxidant in ROS networks under realistic photocatalytic conditions [39]. Table 3 presents the calculated energy values for each reaction involving the $^\bullet O_2^-$(D) species, along with the resulting products.

Table 3. Possible reactions between radical oxygen species with the $^\bullet O_2^-$(D) species as reactive.

Reaction		ΔE (kJ mol^{-1})	ΔG (kJ mol^{-1})
$^\bullet O_2^- + {}^\bullet OH \rightarrow O_2(S) + OH^-$	(5)	−38	−34
$^\bullet O_2^- + H^+ \rightarrow {}^\bullet O_2H$	(6)	130	152

As indicated in Table 3, Reaction (5) exhibits negative ΔE and ΔG values, confirming a thermodynamically favorable process, whereas Reaction (6) shows positive values, indicating that its direct occurrence is not favored. In photocatalytic systems, the formation of $^\bullet O_2H$ is therefore expected to proceed via coupled proton/electron-transfer pathways rather than a single elementary step, in agreement with previous studies [41].

2.2. *OH Species*

Table 4 presents a summary of the thermochemical and molecular properties of the hydroxyl ion OH^-(S) and the hydroxyl radical $^\bullet OH$(D). Between parenthesis, the multiplicity of each species is described (S = singlet and D = doublet). The ($^\bullet$) symbol indicates that the species is radical and the negative sign as super-index indicates that the species has negative charge.

Table 4. Thermochemistry and calculated molecular properties of hydroxyl species.

Species	E° (Hartree)	ΔE° (kJ mol^{-1})	G° (Hartree)	ΔG° (kJ mol^{-1})	$d_{O\text{-}H}$ (Å)	$\nu_{O\text{-}H}$ (cm^{-1})	μ (Debye)	R^2 (Å^2)
OH^-(S)	−75.75	−444	−75.77	−442	0.96	3794	6.23	
$^\bullet OH$(D)	−75.58		−75.60		0.97	3826	2.11	

Formation Reactions of OH Species

The formation of the hydroxyl radical ($^\bullet OH$) from hydrogen peroxide (H_2O_2) involves varying energy requirements depending on the reaction pathway. Figure 2 illustrates the various routes for obtaining both the $^\bullet OH$ and the OH^- ion from H_2O_2. This figure provides a visual representation of the different energy pathways and their respective products, offering a clearer understanding of the reaction mechanisms involved in the formation of these important chemical species.

2.3. *H_2O_2 Species*

H_2O_2 is known as a mild oxidizing agent, capable of oxidizing a variety of organic and inorganic compounds. Interestingly, it is the only stable reactive oxygen species (ROS) and can be specifically detected following the decomposition of other ROS [42,43]. Table 5 details the molecular properties of these three forms of H_2O_2. Notably, the fourth column highlights that the formation of $H_2O_2^-$ is spontaneous, whereas $H_2O_2^+$ formation is non-spontaneous. The structural differences and vibrational frequency values, as shown in this table, stem from their conformational differences.

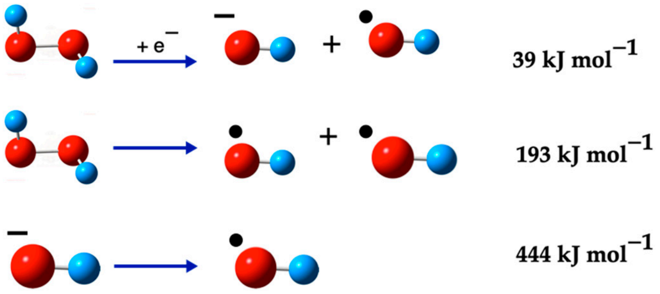

Figure 2. •OH formation from OH− ion and H_2O_2. The red balls are oxygen atoms and small blue balls are hydrogen atoms, the small black ball mark OH as a radical, and the negative sign as super-index indicates that the species has negative charge.

Table 5. Thermochemistry and molecular properties of H_2O_2 species. ΔG° is calculated from the difference between the negative or positive species and the neutral one. The units of bond distances are in Å and the vibrational frequency is in cm^{-1}.

Species	E° (Hartree)	G° (Hartree)	ΔG° ($kJ\ mol^{-1}$)	$d_{O\text{-}O}$ (Å)	$d_{O\text{-}H}$ (Å)	$\nu_{O\text{-}H}$ (cm^{-1})	$\nu_{O\text{-}O}$ (cm^{-1})	μ (Debye)	R^2 (Å^2)
H_2O_2	−151.23	−151.26		1.46	0.97	3799 3803	931	2.48	47.1
$H_2O_2^-$	−151.34	−151.37	−295	2.19	0.97	3854 3857	367	1.55	32.4
$H_2O_2^+$	−151.94	−151.96	773	1.31	1.00	3541	896	3.49	15.8

Figure 3 illustrates the optimized molecular structures for the H_2O_2 species and shows the Gibbs free energy differences between neutral H_2O_2 and the respective ionic forms ($H_2O_2^-$ and $H_2O_2^+$). The computed total spin populations are 1.75 for $H_2O_2^+$ and 0.50 for $H_2O_2^-$.

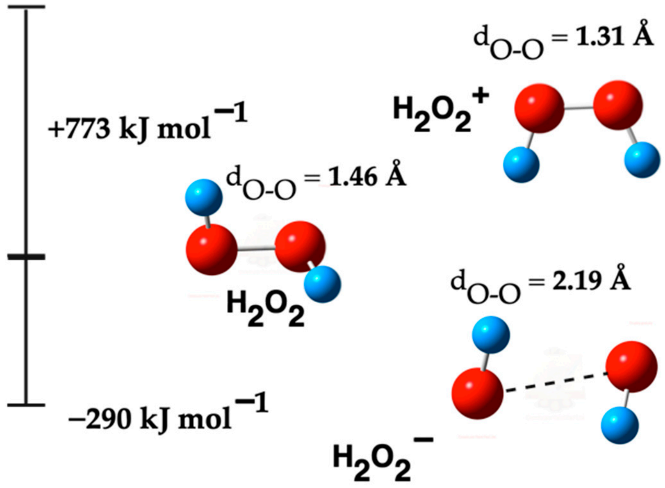

Figure 3. ΔG° of H_2O_2 species. The red balls are oxygen atoms and small blue balls are hydrogen atoms. The dot line in $H_2O_2^-$ species indicates that both oxygen atoms are unbonded.

2.3.1. Formation Reactions of H_2O_2 Species

Hydrogen peroxide (H_2O_2) is typically generated in photocatalysis as a byproduct of water (H_2O) oxidation in the presence of active ROS like hydroxyl radicals (•OH) and superoxide anions (•O_2^-) [44]. In contrast, the Fenton reaction, involving the reduction of H_2O_2 by iron ions (Fe^{2+}) under light, is a pathway for the consumption of preformed H_2O_2 [45–47]. Table 6 summarizes several reactions for H_2O_2 generation.

Table 6. Possible chemical reactions for the generation of H_2O_2.

Reaction		ΔE (kJ mol^{-1})	ΔG (kJ mol^{-1})
$^{\bullet}O_2^{-} + 2H^+ \rightarrow H_2O_2 + h^+$	(7)	542	590
$HO_2^{-} + H_2O \rightarrow H_2O_2 + OH^-$	(8)	492	494
$^{\bullet}O_2H + H^+ \rightarrow H_2O_2 + h^+$	(9)	412	438
$^{\bullet}O_2^{-} + {}^{\bullet}O_2H + H^+ \rightarrow O_2(S) + H_2O_2$	(10)	43	73
$½\,O_2 + H_2O \rightarrow H_2O_2$	(11)	127	142
$^{\bullet}O_2^{-} + {}^{\bullet}O_2H + H_2O \rightarrow H_2O_2 + O_2 + OH^-$	(12)	−45	−40
$^{\bullet}OH + O_2 + OH^- \rightarrow H_2O_2 + O_2^-$	(13)	−31	−2
$^{\bullet}OH + OH^- \rightarrow H_2O_2 + e^-$	(14)	−39	−16
$^{\bullet}OH + {}^{\bullet}OH \rightarrow H_2O_2$	(15)	−193	−163
$^{\bullet}O_2^{-} + 2H^+ + e^- \rightarrow H_2O_2$	(16)	−232	−182
$2H_2O + 2h^+ \rightarrow H_2O_2 + 2H^+$	(17)	−975	−990

The results of this study suggest that Reactions (12) and (16) allow the exergonic formation of H_2O_2 from the superoxide radical ($^{\bullet}O_2^{-}$) radical.

Figure 4 shows the H_2O_2 generation reactions that are presented in Table 6 as thermodynamically favorable (ΔG < 0).

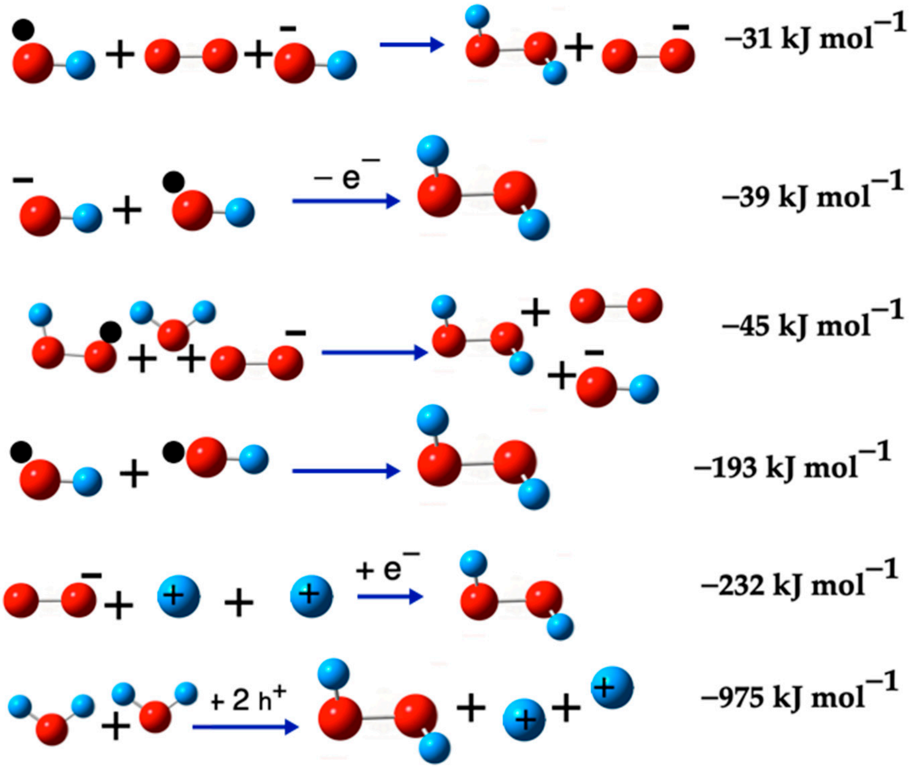

Figure 4. Some H_2O_2 formation reactions. The red balls are oxygen atoms, and the small blue balls are hydrogen atoms, the small black ball marks $^{\bullet}O_2^{-}$(D), $^{\bullet}OH$ and $^{\bullet}O_2H$ as radicals. The O_2(S) is marked with two small black arrows and H+ cation is marked with a + sign.

Figure 5 shows two pathways originating from the superoxide radical $^{\bullet}O_2^{-}$ and require an acidic medium for them to take place. On the one hand, in the presence of an H^+ ion, which can form spontaneously in an aqueous medium, the $^{\bullet}O_2^{-}$ radical reacts with the H^+ ion to form the intermediate species, $^{\bullet}O_2H$ (−45 kJ mol^{-1}). This species then reacts with an H^+ ion and with the superoxide $^{\bullet}O_2^{-}$ present in the medium, to form O_2(S) and H_2O_2 (43 kJ mol^{-1}). On the other hand, the $^{\bullet}O_2^{-}$ radical, two H^+ ions, and one electron led to the spontaneous formation of H_2O_2 (−232 kJ mol^{-1}).

Hence, both pathways for the formation of H_2O_2 require an acidic medium. The presence of a single electron contributes to the spontaneity of these reactions. The main pathways for generating H_2O_2 from the superoxide radical ($^\bullet O_2{}^-$) are illustrated in Figure 5, specifically through Reactions (10), (12), and (16).

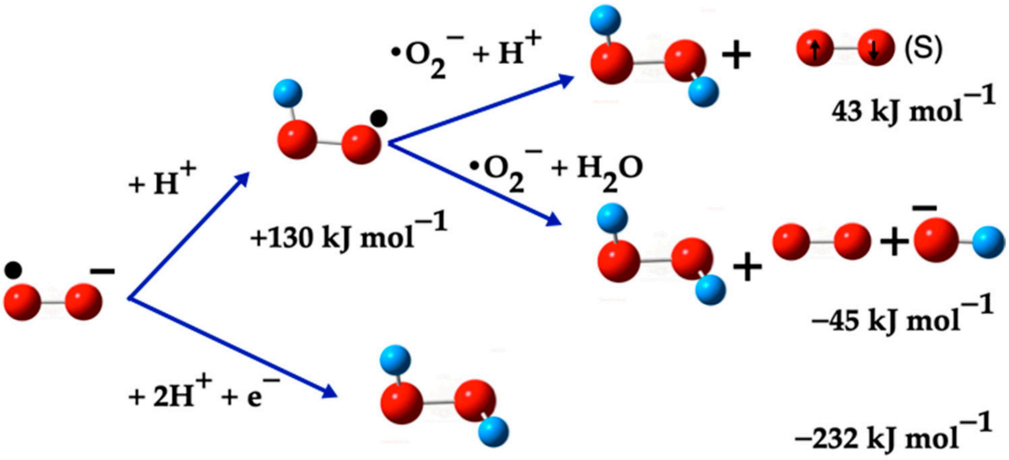

Figure 5. H_2O_2 formation from the $^\bullet O_2{}^-$(D). The red balls are oxygen atoms and small blue balls are hydrogen atoms, the small black ball marks $^\bullet O_2{}^-$(D) and $^\bullet O_2H$ as radicals. The O_2(S) is marked with two small arrows and the (S) symbol.

2.3.2. Dissociation Reactions of H_2O_2 Species

The complexity of ROS studies lies in the numerous possible species and their interactions with electron/hole (e^-/h^+) pairs, leading to the formation, recombination, and dissociation of various ROS due to their high chemical activity. Table 7 outlines some reactions for generating various ROS from H_2O_2 dissociation.

Table 7. Possible chemical reactions for the dissociation of H_2O_2.

Reaction		ΔE (kJ mol^{-1})	ΔG (kJ mol^{-1})
$H_2O_2 \rightarrow {}^\bullet OH + {}^\bullet OH$	(18)	193	163
$H_2O_2 + e^- \rightarrow {}^\bullet OH + OH^-$	(19)	39	16
$H_2O_2 + {}^\bullet O_2{}^- \rightarrow {}^\bullet OH + O_2 + OH^-$	(20)	31	2
$H_2O_2 \rightarrow ½\, O_2 + H_2O$	(21)	−127	−142
$H_2O_2 + h^+ \rightarrow {}^\bullet O_2H + H^+$	(22)	−412	−438
$H_2O_2 + OH^- \rightarrow HO_2{}^- + H_2O$	(23)	−492	−494
$H_2O_2 + h^+ \rightarrow {}^\bullet O_2{}^- + 2H^+$	(24)	−542	−590

Figure 6 visually represents the H_2O_2 dissociation reactions listed in Table 7. Given these results, it can be inferred that in an electron-rich medium, various oxygen radicals interact simultaneously.

2.4. Other Oxygen Species

In this study, the thermochemistry and molecular properties of other radical oxygen species were also calculated. Thus, Table 8 summarizes some common oxygen species typically encountered in systems rich in oxygen radicals.

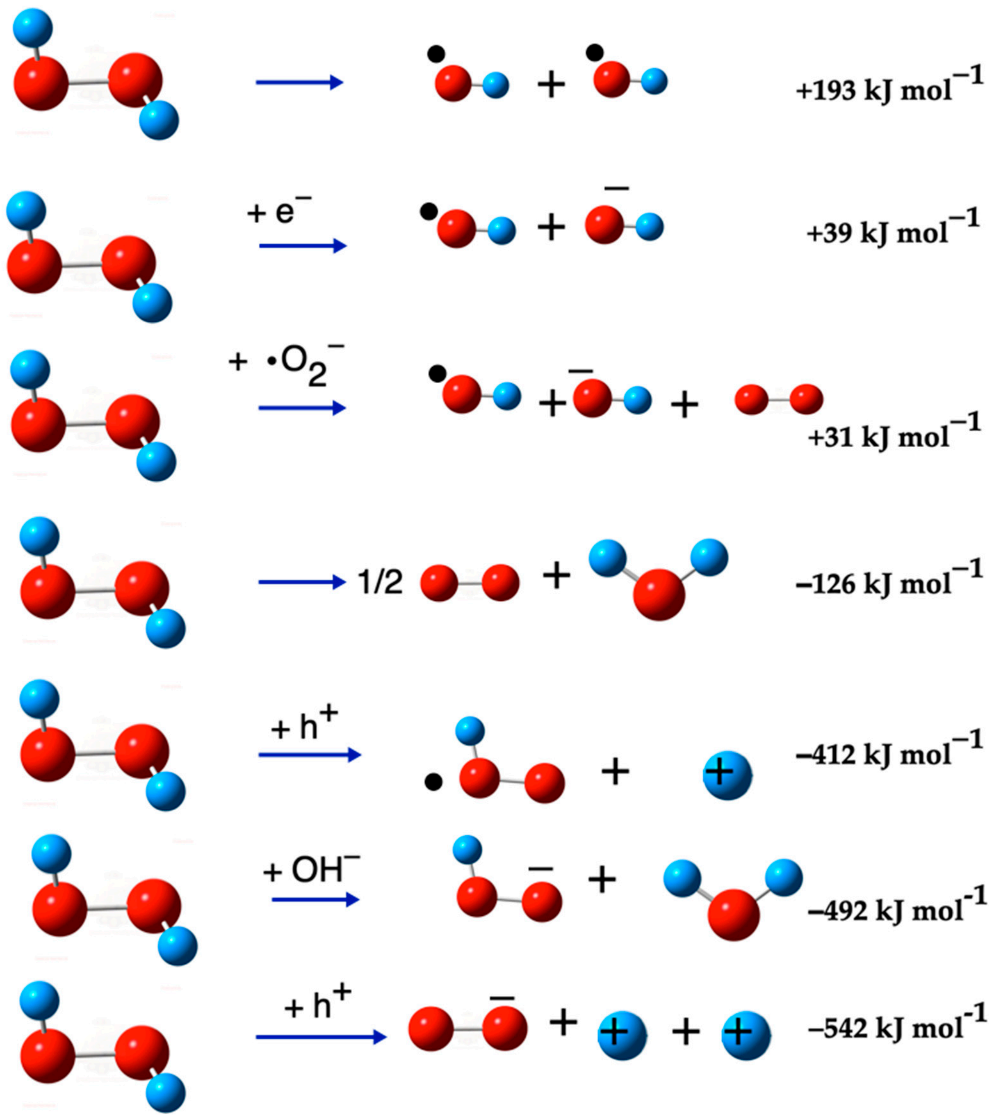

Figure 6. ROS generation from H_2O_2 dissociation. The red balls are oxygen atoms, and the small blue balls are hydrogen atoms, the small black ball marks OH as a radical, and the negative sign as super-index indicates that the species has negative charge.

Table 8. Thermochemistry and molecular properties of several radical oxygen species. ΔG° is calculated from the difference between the negative or positive species and the neutral one. The units of bond distances are in Å and the vibrational frequency is in cm^{-1}.

Species	**E° (Hartree)**	**G° (Hartree)**	**$d_{O\text{-}O}$ (Å)**	**$d_{O\text{-}H}$ (Å)**	**$\nu_{O\text{-}H}$ (cm^{-1})**	**$\nu_{O\text{-}O}$ (cm^{-1})**	**μ (Debye)**	**R^2 (Å^2)**
H^+	−0.50	−0.51					0	3.1
O^-(S)	−75.08	−75.09						4.8
H_2O(S)	−76.26	−76.28		0.96	3844 3952	1626	2.50	29.3
H_2O^+(D)	−75.93	−75.95		1.00	3493 3543	1483	6.28	25.6
$^\bullet O_2H$(D)	−150.60	−150.62	1.33	0.98	3679	1226 1441	2.40	43.9
O_2H^-(S)	−150.74	−150.76	1.51	0.96	3839	1177 891	9.28	50.6

3. Discussion

3.1. O_2 Species

ROS, such as free radicals, are challenging to isolate and characterize experimentally due to their short life and high reactivity [48]. Nonetheless, the computational calculations conducted in this study allow the prediction of thermodynamic properties like Gibbs free energy (G°) and total energy (E°). These properties are decisive for understanding the reactions and behavior of ROS in biological and chemical systems. Molecular oxygen (O_2) is a stable component of air under normal conditions, constituting approximately 20% of its composition [49]. The high-energy electrons in O_2 contribute to their distinctive characteristics. The triplet state of oxygen molecular, O_2(T), exhibits two unpaired electrons in each of its two antibonding π orbitals (πx* and πy*), both at the same energy level. This configuration imparts O_2(T) with notable, although non-extreme, reactivity despite being its ground state [50].

The results present in Table 1 indicate that the superoxide anion ($^{\bullet}O_2^-$) exhibits the highest energetic stability among the evaluated reactive oxygen species (ROS), indicating that its formation is thermodynamically favorable under photocatalytic conditions. Furthermore, its higher dipole moment suggests a stronger interaction with the solvent, which may impact its reactivity in aqueous environments. Table S1 shows a comparison of the thermochemical values and properties of oxygen molecules calculated using both MP2/TZVP and DFT/B3LYP/TZVP.

Partial reduction in molecular oxygen (O_2) can lead to the formation of various reactive oxygen species (ROS). Predominant among these are the superoxide radical, $^{\bullet}O_2^-$(D), in a doublet state, and hydrogen peroxide (H_2O_2), both of which can be successively formed by the reduction of O_2(T) or the single-electron filling of the two π* orbitals. Conversely, singlet oxygen, $^1O_2$(S), is an exceptionally reactive oxygen species generated through a range of chemical and electrochemical reactions. In metal/O_2 batteries, it is hypothesized that singlet oxygen may arise from superoxide disproportionation [51], interactions with byproducts [52], or in the presence of water or protons which can facilitate its formation [51,53]. Photocatalysis can also lead to the gradual oxidation of water resulting in $^1O_2$ production [54]. This excited state of oxygen, with its two unpaired electrons in separate orbitals, is highly reactive. Additionally, as a potent oxidant, $^1O_2$ has a brief half-life, reacting swiftly with proximal compounds, including lipids, proteins, and nucleic acids, before dissipating [55].

In the analysis presented in Table 1, there are visible variations among the molecules in terms of bond distance and vibrational frequencies. However, a notable observation is that they all exhibit the same magnetic moment. This uniformity in magnetic moment suggests a homogeneous distribution of electronic density across these species. Specifically, the electronic spatial extent of the $^{\bullet}O_2^-$(D) radical is observed to be the largest. This is consistent with expectations, as a higher electron density typically leads to an increase in electronic spatial extent. Correspondingly, the O-O bond length in the $^{\bullet}O_2^-$(D) radical is extended, which can be attributed to the electron density effectively pushing the oxygen atoms apart. This increase in bond length is inversely related to the vibrational frequency, leading to its observed decrease.

Formation Reactions of O_2 Species

The energy values from Table 2, indicate that while the formation of $^1O_2$(S) from O_2(T) requires an input of 124 kJ mol^{-1} (Reaction (1)), the subsequent formation of $^{\bullet}O_2^-$(D) from $^1O_2$(S) is spontaneous, releasing almost 400 kJ mol^{-1} (Reaction (2)). For the generation of $^1O_2$(S) from $^{\bullet}O_2^-$(D) (Reaction (3)), the Haber-Weiss reaction has been proposed [56]. However, this reaction has been reported to have a negligible Gibbs energy change compared to the excitation energy of $^1O_2$, suggesting that $^1O_2$ cannot be generated by the Haber-Weiss reaction under these conditions [48]. Alternatively, another pathway (Reaction (4)) that involves an electron (e^-) can spontaneously generate $^\bullet O_2^-$(D) with -281 kJ mol^{-1}. It is important to note that the generation of these species involves both an electron (e^-) and a hole (h^+), typically provided by a semiconductor material with photocatalytic activity. These semiconductors play a critical role in facilitating these chemical reactions.

As can be seen in Figure 1, the formation of singlet oxygen ($^1O_2$) from triplet oxygen (O_2) is a complex process, involving energy transfer from excited photosensitizers to ground-state oxygen molecules. In this process, the photosensitizer absorbs light, becoming excited to a higher energy state, and subsequently transfers energy to a ground-state oxygen molecule, elevating it to a singlet excited state [57,58]. This excited singlet oxygen can undergo intersystem crossover to form a more reactive triplet state, which participates in reactions to generate ROS [59]. Additionally, $^1O_2$ can be generated through the oxidation of superoxide ($^\bullet O_2^-$), where the superoxide ion is oxidized, forming $^1O_2$ and a hydroxyl radical ($^\bullet OH$) [60].

In photocatalysis, the superoxide radical ($^\bullet O_2^-$) is produced by transferring electrons from the photocatalyst to the oxygen molecule adsorbed on the photocatalyst surface, a process known as photoinduced reduction of oxygen [61–63]. This superoxide radical can also be generated by the Fenton reaction, involving the reduction of hydrogen peroxide (H_2O_2) by iron ions (Fe^{2+}) under light [64,65].

Notably, the $^\bullet O_2^-$(D) species exhibits high oxidative activity and participates in multiple reactions. Multiple experiments show that $^\bullet O_2^-$ can dominate oxidative pathways and directly drive contaminant degradation under UV/visible irradiation and co-oxidant assistance. Under visible light, $MoSe_2$/PMS systems identified $^\bullet O_2^-$ as the primary ROS by scavenger tests and EPR, enabling efficient removal of pharmaceuticals/personal-care products; electron-rich/poor dual sites further promote PMS→$^\bullet O_2^-$ conversion [66,67]. In UV/$K_2S_2O_8$ systems, TiO_2 (P25) boosts $O_2 \rightarrow {}^\bullet O_2^-$, overcoming O_2 inhibition and accelerating carbon tetrachloride degradation (without indiscriminate persulfate activation) [68]. S-doped BiOCl with oxygen vacancies strengthens the built-in electric field, amplifying $^\bullet O_2^-$ generation and yielding an 8.8× higher ciprofloxacin degradation rate under visible light [69]. Directional ROS regulation on TiO_2 (e.g., EDTA-2Na) increases azo-dye degradation consistent with larger $^\bullet O_2^-$ contribution [70]. In aerobic photocatalysis, $^\bullet O_2^-$ (with $^1O_2$ and h^+) is verified by EPR/quenching as a primary oxidant for p-nitrophenol on CQDs@Ag_3PO_4 [71]. On nano-TiO_2, the $^\bullet O_2^-$ photogeneration rate correlates with oxygen-vacancy density (chemiluminescence). In Bi@Bi_2MoO_6, metallic Bi and oxygen vacancies enhance O_2^--mediated hydroxylated dichlorination and mineralization of sodium pentachlorophenate [72]. Self-sensitized visible-light degradation of oxytetracycline is strongly inhibited by p-benzoquinone, implicating $^\bullet O_2^-$ in both direct photolysis and TiO_2-assisted routes [73]; and in Ag/TiO_2 heterojunctions, improved carrier separation shifts the dominant oxidant from $^\bullet OH$ (pristine TiO_2) to $^\bullet O_2^-$, enhancing dye oxidation.

3.2. OH Species

The hydroxyl radical ($^\bullet OH$) is a highly reactive and strong oxidizing species, predominantly generated through the oxidation of water (H_2O) in the presence of light and a photocatalyst like TiO_2. In semiconductor photocatalysts, absorption of photons with $h\nu \geq E_g$ promotes electrons from the valence band (VB) to the conduction band (CB), generating electron–hole (e^-/h^+) pairs that relax to the band edges within picoseconds. Band bending at the semiconductor–electrolyte interface and surface trap states assist their spatial/energetic separation, while bulk or surface recombination competes with interfacial redox. CB electrons can reduce dissolved O_2 to $O_2^{\bullet -}$ (and, downstream, form H_2O_2), whereas VB holes oxidize adsorbed H_2O/OH^- to produce $^{\bullet}OH$ (and H^+ when water is the substrate) [74].

The hydroxyl radical ($^{\bullet}OH$) is extremely reactive and short-lived, making its direct detection difficult. On the other hand, $^{\bullet}OH$ plays a crucial role in photocatalytic systems, actively participating in several oxidation pathways that could contribute to both pollutant removal and, under suboptimal conditions, to the formation of transformation byproducts [75]. According to the literature, in aqueous photocatalysis, $^{\bullet}OH$-based AOPs—including TiO_2/UV, UV/H_2O_2, and (photo-)Fenton—achieve high removal and mineralization efficiencies for recalcitrant organics [76]. Representative UV/visible tests with TiO_2 report ≈95% degradation of trichloroethylene (TCE) and tetrachloroethylene (PCE) within ≤150 min using a commercial reactor (Trojan UVMax; emission maxima at 254/436/546 nm), confirming the operational role of $^{\bullet}OH$ in removing chlorinated volatile organic compounds (VOCs); in O_3–TiO_2/UV configurations (365 nm LED), optimization of ozone flow, dose, and irradiance enables near-complete removal of dichloroethylene/trichloroethylene/tetrachloroethylene (DCE/TCE/PCE) while suppressing by-product formation through sufficient $^{\bullet}OH$ generation. Nevertheless, the same extreme reactivity of $^{\bullet}OH$ can promote undesired chlorination pathways in chloride-rich matrices (e.g., addition of $^{\bullet}OH$ to PCE with downstream formation of chlorinated alkanes/phosgene), underscoring the need to control operating conditions and co-oxidants to maximize removal and minimize (re)generation of contaminants [77]. These observations agree with the mechanistic picture of ROS generation/detection reported by others authors and with recent advances that structurally regulate photocatalysts to optimize $^{\bullet}OH$-formation pathways and accelerate rate-limiting steps [21,59], reinforcing the centrality of $^{\bullet}OH$ in removal while explaining its possible contribution to intermediate formation when mineralization is not achieved.

The results shown in Table 4 suggest that under similar conditions, the OH^- ion is more stable than the $^{\bullet}OH$, with the formation of $^{\bullet}OH$ from OH^- requiring almost 450 kJ mol^{-1}. This view is supported by ultrafast RIXS/XFEL experiments in liquid water, which detect $^{\bullet}OH$(aq) only under intense excitation and on fs–ps lifetimes [78]. Under ordinary aqueous conditions, OH^- is the thermodynamically and kinetically dominant species, and $^{\bullet}OH$ emerges only under very strong oxidizing/excitation conditions, in line with our large positive free energy for $OH^- \rightarrow {}^{\bullet}OH$.

While the vibrational frequency values and the O-H bond distance ($d_{\text{O-H}}$) are indistinguishable between the two species, there are significant differences in their magnetic moment and electronic spatial extent. These differences highlight the distinct nature of the OH^- ion and $^{\bullet}OH$, underlining the variability in their stability and reactivity. Table S2 shows a comparison of the thermochemical values and properties of hydroxyl species calculated using both MP2/TZVP and DFT/B3LYP/TZVP.

Formation Reactions of OH Species

Particularly, the generation of $^{\bullet}OH$ from H_2O_2 requires a relatively moderate energy input of 193 kJ mol^{-1}. This energy requirement is significantly lower than the energy needed to form $^{\bullet}OH$ from the hydroxide ion (OH^-), which is about 444 kJ mol^{-1}. However, when H_2O_2 undergoes reduction with an electron, the energy requirement is further reduced to 39 kJ mol^{-1}, making it a more energetically favorable reaction for $^{\bullet}OH$ formation [75]. Apart from these pathways, there exist other routes for generating $^{\bullet}OH$ that require even less energy. However, these alternative pathways often result in the formation of the OH^- ion as a byproduct [42]. This indicates a trade-off between the energy efficiency of the reaction and the purity of the $^{\bullet}OH$ produced.

3.3. H_2O_2 Species

Some reports on the characterization of H_2O_2 species revealed that besides the neutral form (H_2O_2), it has anionic ($H_2O_2^-$) and cationic ($H_2O_2^+$) counterparts. The $H_2O_2^+$ ion can be generated through the removal of an electron from a H_2O_2 molecule, effectively creating a positively charged species. Conversely, the $H_2O_2^-$ ion forms when a H_2O_2 molecule acquires an additional electron, resulting in a negatively charged species. These ionization processes can occur in high-energy environments, such as in photoelectron spectroscopy experiments, or in chemical reactions involving reactive species [79,80]. These forms, particularly $H_2O_2^-$ and $H_2O_2^+$, although less explored but potentially play a significant role in photocatalytic reactions.

The results in Table 5 demonstrate a correlation between electronic charge and bond distance, as well as vibrational frequency. Higher electronic charge results in longer bond distances and higher vibrational frequency values ($\nu_{\text{O-H}}$), alongside lower vibrational frequency values ($\nu_{\text{O-O}}$). Changes in the H-O bond distance ($d_{\text{O-H}}$) across these molecules are not significant. The electronic charge in the $H_2O_2^-$ species causes a notable separation between the oxygen atoms, aligning with findings from another research [81]. Table S3 shows a comparison of the thermochemical values and properties of H_2O_2 species calculated using both MP2/TZVP and DFT/B3LYP/TZVP.

As shown in Figure 3, the cationic ($H_2O_2^+$) and anionic ($H_2O_2^-$) forms of hydrogen peroxide exhibit distinct molecular structures compared to the neutral H_2O_2 molecule. These structural variations arise mainly from the addition or removal of an electron in the H_2O_2 molecule. Thus, the alteration in the electrical charge significantly impacts the distribution of electronic density within the molecule, causing consequent changes in its molecular structure [81].

The comparative analysis of the H_2O_2 species in Figure 3 allows us to clarify the dynamics of photocatalysis, particularly in the context of their roles in environmental remediation processes. The distinct properties of OH^- and $^\bullet OH$, such as stability, reactivity, and electronic characteristics, are key factors that influence their effectiveness in various chemical reactions, including those involved in the degradation of pollutants.

3.3.1. Formation Reactions of H_2O_2 Species

As can be seen in Table 6, the most spontaneous and energetically favorable reactions (Reactions (16) and (17)) involve electrons and holes, whereas reactions involving water and an oxygen molecule (Reaction (11)) or HO_2^- (Reaction (8)) require energy input, consistent with literature findings [82,83]. Notably, the spontaneous formation of H_2O_2 from $^\bullet O_2^-$ in an acidic medium (Reaction (16)) aligns with previous studies. The formation of H_2O_2 from two $^\bullet OH$ (Reaction (15)) is more spontaneous than from an $^\bullet OH$ and an OH^- ion (Reaction (14)), underscoring the higher reactivity of the $^\bullet OH$. The H_2O_2 molecule could be formed from $^\bullet O_2^-$ radical [84] but if there are not electrons and holes (Reactions (7), (10) and (12)), the formation will not be spontaneous.

Within the present theoretical scope, these energy profiles map directly onto experiment-relevant levers for targeted H_2O_2 synthesis: (i) employ mildly acidic electrolytes to supply H^+ and steer $HO_2^\bullet/O_2^{\bullet-}$ speciation toward the exergonic Reaction (16); (ii) maintain high dissolved O_2 and electron-rich operation (illumination/photo-bias or electron-donating environments) to sustain the net two-electron route to H_2O_2 rather than competing pathways; (iii) suppress decomposition by avoiding or passivating Fenton-active sites when $^\bullet OH$ is not the target and by minimizing O–O–cleaving surfaces; and (iv) tune interfacial adsorption/charge to stabilize peroxo-like intermediates without overbinding that would promote O–O cleavage. For benchmarking, H_2O_2 can be quantified with standard assays (including catalase controls) and radical signatures monitored by EPR spin-trapping, while reporting pH, O_2 availability, and light/electron flux to enable comparison with the thermodynamic predictions. These recommendations are consistent with the pH-driven redox/speciation and interfacial adsorption effects documented experimentally for photocatalysis [20].

3.3.2. Dissociation Reactions of H_2O_2 Species

As can be seen in Table 7, dissociation of H_2O_2 with h^+ is spontaneous, often forming water, oxygen, or other species. Reaction (19) indicates that the presence of e^- renders H_2O_2 dissociation non-spontaneous. The spontaneity of certain reactions underscores the necessity of radicals in maintaining ROS in the environment, as exemplified by the interaction of H_2O_2 and OH^- ion yielding water. Furthermore, Reaction (21) suggests that H_2O and O_2 molecules are more stable than H_2O_2, as H_2O_2 spontaneously dissociates into water and molecular oxygen. Conversely, H_2O_2 is more stable than both the $^\bullet OH$ and OH^- ion.

The environment of photochemical reactions that involve reactive oxygen species (ROS) is inherently complex, influenced by various factors such as temperature, impurities, and the composition of the medium. This complexity presents challenges in isolating and analyzing the effects of each factor. For instance, the extremely short lifetimes of these species, the potential for parallel and consecutive reactions, and the influence of photocatalytically active semiconductor materials and radiation sources all contribute to the formation of various reactive species by providing available electrons and holes. These factors can significantly alter the original species, leading to the generation of new ROS [85], some of which are presented in Table 8. Table S4 shows a comparison of the thermochemical values and properties of several radical oxygen species calculated using both MP2/TZVP and DFT/B3LYP/TZVP.

When considering the potential reactions among these species, numerous routes involving ROS in photocatalysis have been hypothesized. However, it is crucial to recognize that the actual reactions occurring near the surface are limited by adsorption phenomena and specific electrical charges. Photocatalysis typically involves simultaneous oxidation and reduction processes, with ROS being produced sequentially from both O_2 and H_2O. For instance, the stepwise oxidation of H_2O can sequentially generate ROS such as hydroxyl radicals ($^\bullet OH$), hydrogen peroxide (H_2O_2), superoxide anion ($^\bullet O_2{}^-$), and singlet oxygen ($^1O_2$). Conversely, the stepwise reduction of O_2 can lead to the formation of species like superoxide anion ($^\bullet O_2{}^-$), hydrogen peroxide (H_2O_2), and hydroxyl radicals ($^\bullet OH$) [86]. This intricate interplay of reactions dictates the overall effectiveness of photocatalytic processes, and therefore a comprehensive understanding of these pathways is essential to optimize photocatalytic systems for environmental and energy applications.

Finally, throughout this work, reactions of ROS formation from various species have been described, as well as dissociation reactions of ROS to form other molecules. Both groups of reactions involve many species. It should not be forgotten that in a photocatalytic system, there are many highly reactive species, such as ROS and, with favorable conditions for high chemical activity, direct and reverse reactions should occur simultaneous, parallel and consecutively, forming multiple species, among others, short-life intermediates; in this scenario, it is very difficult to draw unequivocal conclusions. We summarize the results in Table 9 and Figure 7, highlighting that those reactions are more energetically favored and, therefore, the most probable ones to form the interesting ROS.

Table 9 and Figure 7 show that H_2O_2 appears in the early stages of the ROS cascade. Experimentally, in aqueous photocatalysis, H_2O_2 can arise through two supported routes: (i) two-hole oxidation of interfacial H_2O/OH^- to surface $^\bullet OH$ followed by $2^\bullet OH \rightarrow H_2O_2$ (the net stoichiometry corresponds to Reaction (17)), and (ii) two-electron reduction in dissolved O_2 by conduction-band electrons via $^{\bullet}O_2^-/HO_2^{\bullet} \rightarrow H_2O_2$. Under deoxygenated conditions, route (i) dominates, whereas in aerated solutions route (ii) is often predominant. Apart from $^1O_2$ (formed by energy transfer), H_2O_2 is a key intermediate in the formation of other ROS, but its immediate origin (water vs. oxygen) depends on O_2 levels, pH, and the catalyst surface (phase, trapping/adsorption) [20,87].

Table 9. The most possible chemical reactions for the ROS formation from molecules.

Target ROS	Reaction		ΔE (kJ mol^{-1})	ΔG (kJ mol^{-1})
$^{\bullet}O_2H$	$2H_2O + 2h^+ \rightarrow H_2O_2 + 2H^+$	(17)	−975	−990
	$H_2O_2 + h^+ \rightarrow {}^{\bullet}O_2^- + 2H^+$	(24)	−542	−590
	$^{\bullet}O_2^- + H^+ \rightarrow {}^{\bullet}O_2H$	(6)	+130	+152
			ΔE = −1387	ΔG = −1428
H_2O_2	$2H_2O + 2h^+ \rightarrow H_2O_2 + 2H^+$	(17)	−975	−990
$^{\bullet}O_2^-$	$2H_2O + 2h^+ \rightarrow H_2O_2 + 2H^+$	(17)	−975	−990
	$H_2O_2 + h^+ \rightarrow {}^{\bullet}O_2^- + 2H^+$	(24)	−542	−590
			ΔE = −1517	ΔG = −1580
$^{\bullet}OH$	$2H_2O + 2h^+ \rightarrow H_2O_2 + 2H^+$	(17)	−975	−990
	$H_2O_2 + h^+ \rightarrow {}^{\bullet}O_2^- + 2H^+$	(24)	−542	−590
	$H_2O_2 + {}^{\bullet}O_2^- \rightarrow {}^{\bullet}OH + O_2 + OH^-$	(20)	+31	+2
			ΔE = −1486	ΔG = −1578
$^{\bullet}OH$	$2H_2O + 2h^+ \rightarrow H_2O_2 + 2H^+$	(17)	−975	−990
	$H_2O_2 + e^- \rightarrow {}^{\bullet}OH + OH^-$	(19)	+39	+16
			ΔE = −936	ΔG = −974
$^1O_2$	$O_2 \rightarrow {}^1O_2$	(1)	+124	+126

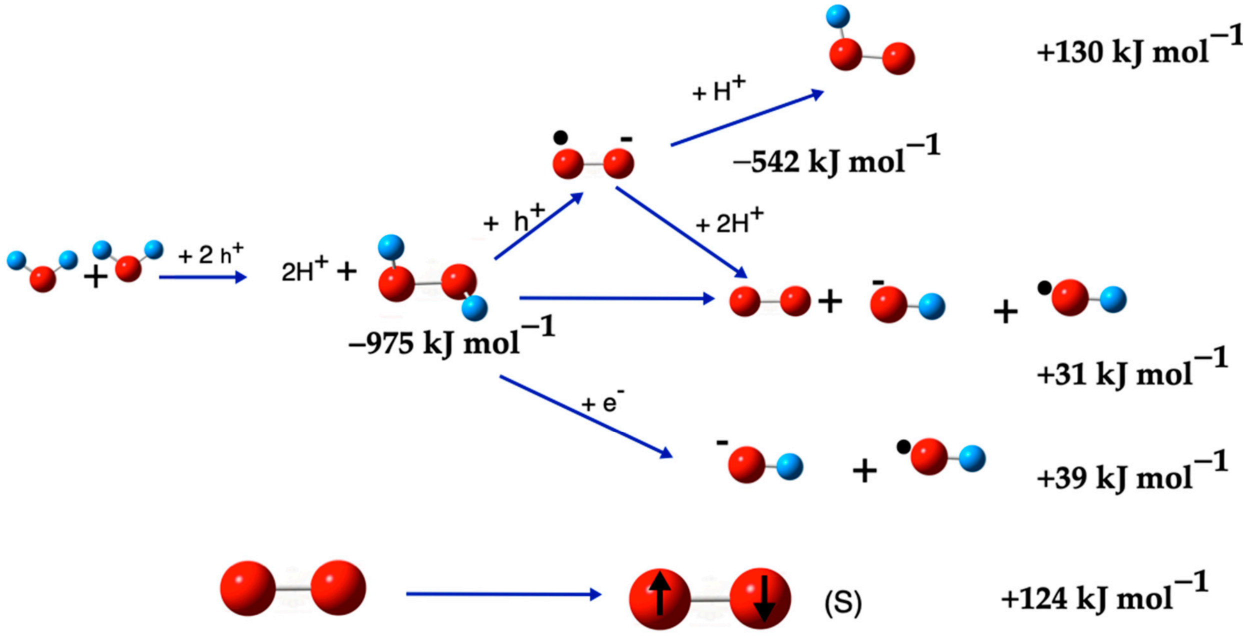

Figure 7. ROS generation from H_2O or O_2 molecules, the energy of each step is indicated, but not the final energy of the full reaction, the total energy is shown in Table 9. The red balls are oxygen atoms and small blue balls are hydrogen atoms, the small black ball mark OH as a radical, and the negative sign as super-index indicates that the species has negative charge.

4. Computational Methods

The study of the formation reactions of various reactive oxygen species (ROS) was conducted using Moller-Pleset 2 (MP2) [88–90] as implemented in Gaussian version 16 software package [91] (Gaussian, Inc., Wallingford, CT, USA) for determine the thermochemical properties of the ROS. This method describes accurately electronic interactions, particularly important in the chemistry of reactive species like ROS [92–95].

In this study, second-order Møller–Plesset perturbation theory (MP2) was prioritized for mapping the thermodynamics of ROS, as it provides an explicit description of dynamic electron correlation and has demonstrated accuracy and computational efficiency [38]. MP2 serves as a post-Hartree–Fock alternative when approximate DFT functionals can incur self-interaction and delocalization errors in charge-separated radical states [96]. In this context, for the small ROS described in this study, MP2 offers a favorable balance between accuracy and cost and produces thermodynamic trends consistent with a lower functional dependence on aqueous solvation [97]. The Supplementary Materials (Tables S1–S4) comparatively document the thermochemistry and molecular properties of MP2/TZVP and DFT/B3LYP/TZVP.

The molecular properties of the species studied were computed using the Ahlrichs et al. basis set, specifically the triple-zeta valence with polarization (TZVP) basis set [98,99]. This set was chosen for its ability to accurately represent the electronic structure of the species. The TZVP basis set is optimized to balance the precision of valence orbital descriptions with computational efficiency [100]. This approach ensures a reliable depiction of key elements, allowing for accurate predictions regarding the stability and reactivity of the species. The choice of the TZVP basis set underpins the reliability of this study, providing precise insights into the molecular properties of reactive oxygen species (ROS).

In this study, the root mean square convergence criterion for the density matrix in the self-consistent field (SCF) iteration was set to 10^{-14} a.u., aiming for an energy convergence threshold of at least 10^{-15} a.u. (GAUSSIAN keyword: SCF = tight). This default convergence criteria recommended by Gaussian 16 were applied to ensure the reliability and precision in the calculations. These criteria ensure that the resulting structures represent appropriate energy minima, which is an important aspect for studies aiming to understand the stability and reaction pathways of ROS. It is worth mentioning that the total energy, defined here as the sum of all electronic contributions plus zero-point energy corrections, is an important metric to evaluate the thermodynamic stability and chemical reactivity of ROS. The precision in the determination of the total energy allows direct comparisons between different chemical species and the evaluation of possible reaction pathways and mechanisms.

After the geometric optimization of the molecules, which aims to locate the structures at their most stable energy minima, it proceeded with the calculation of the vibrational frequencies. Vibrational frequency calculations are critical for confirming that optimized geometries represent true energy minima, as indicated by the absence of imaginary frequencies. These calculations provide insights into molecular stability and potential reaction mechanisms, enhancing our understanding of ROS dynamics. Secondly, it provides valuable insights into molecular dynamics, allowing a better understanding of how ROS interact and react in various contexts. The vibrational frequencies were calculated by applying the principle of harmonic oscillation, which assumes that molecular vibrations near equilibrium can be modeled as harmonic oscillators. Gaussian 16 uses advanced algorithms to determine force constants from which frequencies are calculated.

The analysis of vibrational frequencies offers detailed information on the rigidity of molecular bonds and the stability of structures. Higher frequencies indicate stronger bonds and more rigid structures, while lower frequencies may indicate weaker bonds or more flexible molecular groups. This analysis is complemented by the calculation of the zero-point energy (ZPE) and thermal corrections to thermodynamic properties such as enthalpy and Gibbs free energy, which are critical to understanding the thermodynamics of the reactions in which ROS participate. By integrating the Polarizable Continuum Model (PCM), it was possible to assess the impact of the solvent environment on vibrational frequencies, which is crucial for accurate simulations of molecular dynamics in aqueous solutions.

The PCM simulates the solvent as a continuous polarizable medium surrounding the solute, automatically generating a virtual cavity based on the molecular geometry of the study molecule, ensuring an accurate representation of the polarizing effect of the solvent. The selection of water as a solvent in all simulations was based on its relevance in biological and photocatalytic processes [20]. Gaussian 16 allows water to be specified as a solvent by adjusting its dielectric constant ($\varepsilon = 78.4$), together with the surface tension and other relevant solvent parameters, to values characteristic of water at room temperature. These adjustments are essential to align the simulations with real experimental conditions, ensuring that the computational findings are applicable and relevant to the analysis of ROS interactions and reactions under typical experimental conditions [101,102].

Finally, visualization of all molecular structures and properties was enabled by the GaussView version 6 software package (Semichem Inc., Shawnee Mission, KS, USA) [103].

5. Conclusions

In this computational study, the different molecular oxygen (O_2) species were examined, including O_2(T) in its triplet state, $^1O_2$(S) in its singlet state, and $^\bullet O_2{}^-$(D) in its negatively charged doublet state. The results indicate that these species possess similar molecular properties, such as bond lengths and dipole moments, suggesting a uniform distribution of electron density across these molecules. However, notable distinctions in bond distances and vibrational frequencies were observed, which may significantly impact their reactivity and chemical behavior. A key finding is that the $^\bullet O_2{}^-$(D) species exhibits the largest electronic spatial extent, aligning with its increased electron density due to its negative charge. This attribute potentially renders it highly reactive in chemical reactions.

In terms of the interconversion of these molecular oxygen species, this study reveals that the transformation from O_2(T) to O_2(S) requires energy, indicating its non-spontaneity under the examined conditions. Conversely, the conversion of O_2(S) to $^\bullet O_2{}^-$(D) is a spontaneous reaction, releasing substantial energy, approximately 400 kJ mol^{-1}.

This research also examined hydrogen peroxide (H_2O_2) in its neutral, anionic, and cationic forms, revealing marked differences in their thermodynamic feasibility that depend on the surrounding environment. Computed maps indicate that the anionic pathway is thermodynamically accessible under electron-rich conditions and is favored at alkaline pH (H_2O_2/HOO^- speciation), whereas the cationic form is disfavored, consistent with its expected rarity. Within the theoretical scope adopted here, the exergonic H_2O_2-formation routes are consistent with pH-driven redox/speciation and interfacial adsorption/charge effects reported experimentally, thereby delineating clear levers for benchmarking: pH control (mildly acidic to accumulate H_2O_2; alkaline to probe HOO^-), dissolved O_2 availability, and surface properties (adsorption/charge) that stabilize peroxo-like intermediates [20]. For experimental verification, validation can rely on standard H_2O_2 assays (with catalase controls) and EPR spin-trapping for radicals; reporting operating parameters (pH, O_2, light/electron flux) is recommended to enable direct comparison with the present thermodynamic predictions [20].

The study further explored a range of radical oxygen species present in ROS-rich systems, defined by elevated interfacial production and higher steady-state levels of ROS ($^\bullet$OH, $^\bullet O_2{}^-$/$HO_2{}^\bullet$, H_2O_2, $^1O_2$) relative to dark or no-catalyst controls. A diversity of molecular properties was observed among these species, including variations in bond lengths, vibrational frequencies, and dipole moments. The presence of H^+ ions, indicative of medium acidity, appears to be a critical factor influencing many reactions involving these species. Additionally, we investigated potential reactions among these radical oxygen species, particularly focusing on the highly reactive ${}^{\bullet}O_2{}^{-}$(D) species. A variety of reactions, leading to both spontaneous and non-spontaneous products, was observed, emphasizing the intricate network of chemical interactions in environments rich in oxygen radicals.

Finally, the results of this study provide an intrinsic aqueous-phase thermodynamic map ($\Delta E/\Delta G$) and molecular descriptors for key ROS (${}^{\bullet}OH$, ${}^{\bullet}O_2{}^{-}/HO_2{}^{\bullet}$, H_2O_2, ${}^{1}O_2$), identifying exergonic vs. endergonic steps and the pH-conditioned speciation that govern their interconversion. Although derived for air-saturated water at 298 K without explicit surfaces, this baseline constrains which pathways are thermodynamically feasible in chemically and biologically complex milieus, where microenvironmental pH/[H^+], O_2 availability, interfacial adsorption, and metal centers (e.g., Fe/Cu) modulate kinetics and selectivity. The framework therefore offers testable predictions and design guidance for photocatalytic and AOP settings (e.g., UVA-driven semiconductor interfaces or UVC/UV–H_2O_2 systems) and a quantitative basis for interpreting ROS-mediated processes in cells and environmental matrices.

Supplementary Materials: The following supporting information can be downloaded at: https://www.mdpi.com/article/10.3390/ijms26188989/s1.

Author Contributions: Conceptualization, S.G. and X.J.-F.; methodology, S.G. and X.J.-F.; software, S.G. and X.J.-F.; validation, S.G. and X.J.-F.; formal analysis, S.G. and X.J.-F.; investigation, S.G. and X.J.-F.; resources, S.G. and X.J.-F.; data curation, S.G. and X.J.-F.; writing—original draft preparation, S.G. and X.J.-F.; writing—review and editing, S.G. and X.J.-F.; visualization, S.G. and X.J.-F.; supervision, S.G. and X.J.-F.; project administration, S.G. and X.J.-F.; funding acquisition, S.G. and X.J.-F. All authors have read and agreed to the published version of the manuscript.

Funding: The APC was funded by Universidad Técnica Particular de Loja (UTPL), grant number 3000.

Institutional Review Board Statement: Not applicable.

Informed Consent Statement: Not applicable.

Data Availability Statement: Data are available within the article.

Acknowledgments: The authors would like to thank the Universidad Técnica Particular de Loja (UTPL) for the computing time on the High-Performance Computing (HPC) server.

Conflicts of Interest: The authors declare no conflicts of interest.

Abbreviations

The following abbreviations are used in this manuscript:

ROS	Reactive Oxygen Species
${}^{\bullet}O_2{}^{-}$	Superoxide anion radical
H_2O_2	Hydrogen peroxide
${}^{1}O_2$	Singlet oxygen
${}^{\bullet}OH$	Hydroxyl radical
$H_2O_2{}^{+}$	Protonated hydrogen peroxide
$H_2O_2{}^{-}$	Deprotonated hydrogen peroxide
OH^{-}	Hydroxide ion
H^{+}	Hydrogen ion or proton
H_2O	Water
$HO_2{}^{-}$	Perhydroxide ion
${}^{\bullet}O_2H$	Hydroperoxyl radical
e^{-}	Electron
h^{+}	Hole

T	Triplet state
S	Singlet state
D	Doublet state
G°, E°	Standard Gibbs free energy and total energy
ΔG	Change in Gibbs Free Energy
ΔE	Change in Energy
ΔG^0	Standard change in Gibbs Free Energy
dO-O, dO-H	Bond distances between O atoms and between O and H atoms
νO-O, νO-H	Vibrational frequencies of O-O and O-H bonds
μ	Dipole moment
R^2	Electronic spatial extent
ZPE	Zero-Point Energy
B3LYP	Becke, 3-parameter, Lee-Yang-Parr
SCF	Self-Consistent Field
PCM	Polarizable Continuum Model
MP2	Moller-Pleset 2

References

1. Ong, W.-J.J.W.; Maeda, K. *Emerging Nanomaterials for Light-Driven Reactions: Past, Present, and Future*; John Wiley & Sons, Ltd.: Hoboken, NJ, USA, 2020; Volume 4, p. 2000354.
2. Ortiz, I.; Rivero, M.J.; Margallo, M. Advanced oxidative and catalytic processes. In *Sustainable Water and Wastewater Processing*; Elsevier: Amsterdam, The Netherlands, 2019; pp. 161–201; ISBN 9780128161708.
3. Schneider, J.; Matsuoka, M.; Takeuchi, M.; Zhang, J.; Horiuchi, Y.; Anpo, M.; Bahnemann, D.W. Understanding TiO_2 Photocatalysis: Mechanisms and Materials. *Chem. Rev.* **2014**, *114*, 9919–9986. [CrossRef] [PubMed]
4. Zhu, S.; Wang, D. *Photocatalysis: Basic Principles, Diverse Forms of Implementations and Emerging Scientific Opportunities*; John Wiley & Sons, Ltd.: Hoboken, NJ, USA, 2017; Volume 7, p. 1700841.
5. Wang, J.; Wang, S. *Reactive Species in Advanced Oxidation Processes: Formation, Identification and Reaction Mechanism*; Elsevier: Amsterdam, The Netherlands, 2020; Volume 401, p. 126158.
6. Jaramillo-Fierro, X.; Cuenca, M.F. Novel Semiconductor $Cu(C_3H_3N_3S_3)_3/ZnTiO_3/TiO_2$ for the Photoinactivation of *E. coli* and *S. aureus* under Solar Light. *Nanomaterials* **2023**, *13*, 173. [CrossRef]
7. Hamblin, M.R.; Abrahamse, H. Oxygen-Independent Antimicrobial Photoinactivation: Type III Photochemical Mechanism? *Antibiotics* **2020**, *9*, 53. [CrossRef] [PubMed]
8. Laxma Reddy, P.V.; Kavitha, B.; Kumar Reddy, P.A.; Kim, K.H. *TiO2-Based Photocatalytic Disinfection of Microbes in Aqueous Media: A Review*; Academic Press: Cambridge, MA, USA, 2017; Volume 154, pp. 296–303.
9. Rettig, I.D.; McCormick, T.M. *Enrolling Reactive Oxygen Species in Photon-to-Chemical Energy Conversion: Fundamentals, Technological Advances, and Applications*; Taylor & Francis: Abingdon, UK, 2021; Volume 6, p. 1950049.
10. Saravanan, A.; Kumar, P.S.; Jeevanantham, S.; Karishma, S.; Kiruthika, A.R. Photocatalytic disinfection of micro-organisms: Mechanisms and applications. *Environ. Technol. Innov.* **2021**, *24*, 101909. [CrossRef]
11. Kong, L.; Zepp, R.G. Production and consumption of reactive oxygen species by fullerenes. *Environ. Toxicol. Chem.* **2012**, *31*, 136–143. [CrossRef] [PubMed]
12. Ding, L.; Li, M.; Zhao, Y.; Zhang, H.; Shang, J.; Zhong, J.; Sheng, H.; Chen, C.; Zhao, J. The vital role of surface Brönsted acid/base sites for the photocatalytic formation of free ·OH radicals. *Appl. Catal. B Environ.* **2020**, *266*, 118634. [CrossRef]
13. Shen, J.; Li, Z.-J.; Hang, Z.-F.; Xu, S.-F.; Liu, Q.-Q.; Tang, H.; Zhao, X.-W. Insights into the Effect of Reactive Oxygen Species Regulation on Photocatalytic Performance via Construction of a Metal-Semiconductor Heterojunction. *J. Nanosci. Nanotechnol.* **2020**, *20*, 3478–3485. [CrossRef]
14. Sun, Y.; Guo, S.-Q.; Fan, L.; Cai, J.; Han, W.; Zhang, F. Molecular oxygen activation in photocatalysis: Generation, detection and application. *Surf. Interfaces* **2024**, *46*, 104033. [CrossRef]
15. González, S.; Jaramillo-Fierro, X. Density Functional Theory Study of Methylene Blue Demethylation as a Key Step in Degradation Mediated by Reactive Oxygen Species. *Int. J. Mol. Sci.* **2025**, *26*, 1756. [CrossRef]
16. Winterbourn, C.C. Biological chemistry of superoxide radicals. *ChemTexts* **2020**, *6*, 7. [CrossRef]
17. Flores-López, L.Z.; Espinoza-Gómez, H.; Somanathan, R. *Silver Nanoparticles: Electron Transfer, Reactive Oxygen Species, Oxidative Stress, Beneficial and Toxicological Effects. Mini Review*; John Wiley & Sons, Ltd.: Hoboken, NJ, USA, 2019; Volume 39, pp. 16–26.
18. Hou, H.; Zeng, X.; Zhang, X. Production of Hydrogen Peroxide by Photocatalytic Processes. *Angew. Chem. Int. Ed.* **2020**, *59*, 17356–17376. [CrossRef]

19. Lu, X.; Qiu, W.; Ma, J.; Xu, H.; Wang, D.; Cheng, H.; Zhang, W.; He, X. The overestimated role of singlet oxygen for pollutants degradation in some non-photochemical systems. *Chem. Eng. J.* **2020**, *401*, 126128. [CrossRef]
20. Nosaka, Y.; Nosaka, A.Y. Generation and Detection of Reactive Oxygen Species in Photocatalysis. *Chem. Rev.* **2017**, *117*, 11302–11336. [CrossRef]
21. Nosaka, Y.; Nosaka, A. *Understanding Hydroxyl Radical ($^{\bullet}$OH) Generation Processes in Photocatalysis*; American Chemical Society: New York, NY, USA, 2016; Volume 1, pp. 356–359.
22. Zhu, S.; Zheng, W.; Duan, W.; Feng, C. Reaction: Harnessing reactive oxygen species (ROS) for water purification. *Chem* **2023**, *9*, 1340–1341. [CrossRef]
23. Bi, Z.; Wang, W.; Zhao, L.; Wang, X.; Xing, D.; Zhou, Y.; Lee, D.-J.; Ren, N.; Chen, C. The generation and transformation mechanisms of reactive oxygen species in the environment and their implications for pollution control processes: A review. *Environ. Res.* **2024**, *260*, 119592. [CrossRef]
24. Edalati, P.; Itagoe, Y.; Ishihara, H.; Ishihara, T.; Emami, H.; Arita, M.; Fuji, M.; Edalati, K. Visible-light photocatalytic oxygen production on a high-entropy oxide by multiple-heterojunction introduction. *J. Photochem. Photobiol. A Chem.* **2022**, *433*, 114167. [CrossRef]
25. Foglietta, F.; Serpe, L.; Canaparo, R. ROS-generating nanoplatforms as selective and tunable therapeutic weapons against cancer. *Discov. Nano* **2023**, *18*, 151. [CrossRef] [PubMed]
26. Khan, S.; Raja, M.A.; Sayed, M.; Shah, L.A.; Sohail, M. Advanced Oxidation and Reduction Processes. In *Advances in Water Purification Techniques: Meeting the Needs of Developed and Developing Countries*; Elsevier: Amsterdam, The Netherlands, 2019; pp. 135–164; ISBN 9780128147900.
27. Feng, D.; Li, X.; Liu, Y.; Chen, X.; Li, S. Emerging Bismuth-Based Step-Scheme Heterojunction Photocatalysts for Energy and Environmental Applications. *Renewables* **2023**, *1*, 485–513. [CrossRef]
28. Zhang, J.; Yu, G.; Yang, C.; Li, S. Recent progress on S-scheme heterojunction strategy enabling polymer carbon nitrides C3N4 and C3N5 enhanced photocatalysis in energy conversion and environmental remediation. *Curr. Opin. Chem. Eng.* **2024**, *45*, 101040. [CrossRef]
29. Jaramillo-Fierro, X.; Cuenca, G.; Ramón, J. Comparative Study of the Effect of Doping ZnTiO3 with Rare Earths (La and Ce) on the Adsorption and Photodegradation of Cyanide in Aqueous Systems. *Int. J. Mol. Sci.* **2023**, *24*, 3780. [CrossRef]
30. Li, Y.; Liao, C.; Tjong, S.C. Recent Advances in Zinc Oxide Nanostructures with Antimicrobial Activities. *Int. J. Mol. Sci.* **2020**, *21*, 8836. [CrossRef]
31. Li, Q.; Li, F.T. Recent advances in molecular oxygen activation via photocatalysis and its application in oxidation reactions. *Chem. Eng. J.* **2021**, *421*, 129915. [CrossRef]
32. Litter, M.I. *Introduction to Oxidative Technologies for Water Treatment*; Springer: Cham, Switzerland, 2020; pp. 119–175.
33. Luo, L.; Zhang, T.; Wang, M.; Yun, R.; Xiang, X. Recent Advances in Heterogeneous Photo-Driven Oxidation of Organic Molecules by Reactive Oxygen Species. *ChemSusChem* **2020**, *13*, 5173–5184. [CrossRef]
34. Cai, M.; Liu, Y.; Dong, K.; Chen, X.; Li, S. Floatable S-scheme Bi2WO6/C3N4/carbon fiber cloth composite photocatalyst for efficient water decontamination. *Chin. J. Catal.* **2023**, *52*, 239–251. [CrossRef]
35. Yang, J.; Li, Y.; Yang, Z.; Ying, G.-G.; Shih, K.; Feng, Y. Hydrogen peroxide as a key intermediate for hydroxyl radical generation during catalytic ozonation of biochar: Mechanistic insights into the evolution and contribution of radicals. *Sep. Purif. Technol.* **2023**, *324*, 124525. [CrossRef]
36. Liu, J.; Dong, G.; Jing, J.; Zhang, S.; Huang, Y.; Ho, W. Photocatalytic reactive oxygen species generation activity of TiO2 improved by the modification of persistent free radicals. *Environ. Sci. Nano* **2021**, *8*, 3846–3854. [CrossRef]
37. Vuckovic, S.; Fabiano, E.; Gori-Giorgi, P.; Burke, K. MAP: An MP2 Accuracy Predictor for Weak Interactions from Adiabatic Connection Theory. *J. Chem. Theory Comput.* **2020**, *16*, 4141–4149. [CrossRef]
38. Shang, H.; Yang, J. Implementation of Laplace Transformed MP2 for Periodic Systems with Numerical Atomic Orbitals. *Front. Chem.* **2020**, *8*, 589992. [CrossRef] [PubMed]
39. Andrés, C.M.C.; Pérez de la Lastra, J.M.; Andrés Juan, C.; Plou, F.J.; Pérez-Lebeña, E. Superoxide Anion Chemistry—Its Role at the Core of the Innate Immunity. *Int. J. Mol. Sci.* **2023**, *24*, 1841. [CrossRef]
40. Peng, Y.; Bian, Z.; Wang, F.; Li, S.; Xu, S.; Wang, H. Electrocatalytic degradation of p-nitrophenol on metal-free cathode: Superoxide radical (O2•−) production via molecular oxygen activation. *J. Hazard. Mater.* **2024**, *462*, 132797. [CrossRef]
41. Chen, Z.; Yao, D.; Chu, C.; Mao, S. Photocatalytic H_2O_2 production Systems: Design strategies and environmental applications. *Chem. Eng. J.* **2023**, *451*, 138489. [CrossRef]
42. Gao, J.; Yang, H.b.; Huang, X.; Hung, S.F.; Cai, W.; Jia, C.; Miao, S.; Chen, H.M.; Yang, X.; Huang, Y.; et al. Enabling Direct H_2O_2 Production in Acidic Media through Rational Design of Transition Metal Single Atom Catalyst. *Chem* **2020**, *6*, 658–674. [CrossRef]
43. Wang, L.; Li, B.; Dionysiou, D.D.; Chen, B.; Yang, J.; Li, J. Overlooked Formation of H_2O_2 during the Hydroxyl Radical-Scavenging Process When Using Alcohols as Scavengers. *Environ. Sci. Technol.* **2022**, *56*, 3386–3396. [CrossRef] [PubMed]

44. Mahne, N.; Schafzahl, B.; Leypold, C.; Leypold, M.; Grumm, S.; Leitgeb, A.; Strohmeier, G.A.; Wilkening, M.; Fontaine, O.; Kramer, D.; et al. Singlet oxygen generation as a major cause for parasitic reactions during cycling of aprotic lithium-oxygen batteries. *Nat. Energy* **2017**, *2*, 17036. [CrossRef]
45. Dalrymple, R.M.; Carfagno, A.K.; Sharpless, C.M. Correlations between dissolved organic matter optical properties and quantum yields of singlet oxygen and hydrogen peroxide. *Environ. Sci. Technol.* **2010**, *44*, 5824–5829. [CrossRef]
46. Hayyan, M.; Hashim, M.A.; Alnashef, I.M. Superoxide Ion: Generation and Chemical Implications. *Chem. Rev.* **2016**, *116*, 3029–3085. [CrossRef]
47. Khan, A.U.; Kasha, M. Singlet molecular oxygen in the Haber-Weiss reaction. *Proc. Natl. Acad. Sci. USA* **1994**, *91*, 12365–12367. [CrossRef]
48. Wandt, J.; Freiberg, A.T.S.; Ogrodnik, A.; Gasteiger, H.A. Singlet oxygen evolution from layered transition metal oxide cathode materials and its implications for lithium-ion batteries. *Mater. Today* **2018**, *21*, 825–833. [CrossRef]
49. Zhang, X.F.; Zhu, J. BODIPY parent compound: Excited triplet state and singlet oxygen formation exhibit strong molecular oxygen enhancing effect. *J. Lumin.* **2019**, *212*, 286–292. [CrossRef]
50. Yanai, N.; Kimizuka, N. New Triplet Sensitization Routes for Photon Upconversion: Thermally Activated Delayed Fluorescence Molecules, Inorganic Nanocrystals, and Singlet-to-Triplet Absorption. *Acc. Chem. Res.* **2017**, *50*, 2487–2495. [CrossRef] [PubMed]
51. Pospíšil, P.; Prasad, A.; Rác, M. Mechanism of the formation of electronically excited species by oxidative metabolic processes: Role of reactive oxygen species. *Biomolecules* **2019**, *9*, 258. [CrossRef]
52. Petit, Y.K.; Mourad, E.; Prehal, C.; Leypold, C.; Windischbacher, A.; Mijailovic, D.; Slugovc, C.; Borisov, S.M.; Zojer, E.; Brutti, S.; et al. Mechanism of mediated alkali peroxide oxidation and triplet versus singlet oxygen formation. *Nat. Chem.* **2021**, *13*, 465–471. [CrossRef] [PubMed]
53. Kőrösi, L.; Bognár, B.; Bouderias, S.; Castelli, A.; Scarpellini, A.; Pasquale, L.; Prato, M. Highly-efficient photocatalytic generation of superoxide radicals by phase-pure rutile TiO_2 nanoparticles for azo dye removal. *Appl. Surf. Sci.* **2019**, *493*, 719–728. [CrossRef]
54. Yu, W.; Chen, F.; Wang, Y.; Zhao, L. Rapid evaluation of oxygen vacancies-enhanced photogeneration of the superoxide radical in nano-TiO2suspensions. *RSC Adv.* **2020**, *10*, 29082–29089. [CrossRef]
55. Li, X.; Lyu, S.; Lang, X. Superoxide generated by blue light photocatalysis of g-C_3N_4/TiO_2 for selective conversion of amines. *Environ. Res.* **2021**, *195*, 110851. [CrossRef] [PubMed]
56. Pan, Y.; Su, H.; Zhu, Y.; Vafaei Molamahmood, H.; Long, M. CaO_2 based Fenton-like reaction at neutral pH: Accelerated reduction of ferric species and production of superoxide radicals. *Water Res.* **2018**, *145*, 731–740. [CrossRef] [PubMed]
57. Yi, Q.; Ji, J.; Shen, B.; Dong, C.; Liu, J.; Zhang, J.; Xing, M. Singlet Oxygen Triggered by Superoxide Radicals in a Molybdenum Cocatalytic Fenton Reaction with Enhanced REDOX Activity in the Environment. *Environ. Sci. Technol.* **2019**, *53*, 9725–9733. [CrossRef]
58. Zaichenko, A.; Schröder, D.; Janek, J.; Mollenhauer, D. Pathways to Triplet or Singlet Oxygen during the Dissociation of Alkali Metal Superoxides: Insights by Multireference Calculations of Molecular Model Systems. *Chem. A Eur. J.* **2020**, *26*, 2395–2404. [CrossRef]
59. Yang, L.; Chen, Z.; Cao, Q.; Liao, H.; Gao, J.; Zhang, L.; Wei, W.; Li, H.; Lu, J. Structural Regulation of Photocatalyst to Optimize Hydroxyl Radical Production Pathways for Highly Efficient Photocatalytic Oxidation. *Adv. Mater.* **2024**, *36*, 2306758. [CrossRef]
60. Liu, Y.; Zhao, Y.; Wang, J. Fenton/Fenton-like processes with in-situ production of hydrogen peroxide/hydroxyl radical for degradation of emerging contaminants: Advances and prospects. *J. Hazard. Mater.* **2021**, *404*, 124191. [CrossRef]
61. Litorja, M.; Ruscic, B. A photoionization study of the hydroperoxyl radical, HO_2, and hydrogen peroxide, H_2O_2. *J. Electron Spectros. Relat. Phenom.* **1998**, *97*, 131–146. [CrossRef]
62. Thürmer, S.; Unger, I.; Slavíček, P.; Winter, B. Relaxation of Electronically Excited Hydrogen Peroxide in Liquid Water: Insights from Auger-Electron Emission. *J. Phys. Chem. C* **2013**, *117*, 22268–22275. [CrossRef]
63. Hrušák, J.; Iwata, S. The vibrational spectrum of $H_2O_2{}^+$ radical cation: An illustration of symmetry breaking. *J. Chem. Phys.* **1997**, *106*, 4877–4888. [CrossRef]
64. Thompson, W.E.; Lugez, C.L.; Jacox, M.E. The infrared spectrum of $HOOH^+$ trapped in solid neon. *J. Chem. Phys.* **2012**, *137*, 144305. [CrossRef]
65. Messer, B.M.; Stielstra, D.E.; Cappa, C.D.; Scholtens, K.W.; Elrod, M.J. Computational and experimental studies of chemical ionization mass spectrometric detection techniques for atmospherically relevant peroxides. *Int. J. Mass Spectrom.* **2000**, *197*, 219–235. [CrossRef]
66. Dong, C.; Wang, Z.; Ye, Z.; He, J.; Zheng, Z.; Gong, X.; Zhang, J.; Lo, I.M.C. Superoxide radicals dominated visible light driven peroxymonosulfate activation using molybdenum selenide (MoSe2) for boosting catalytic degradation of pharmaceuticals and personal care products. *Appl. Catal. B Environ.* **2021**, *296*, 120223. [CrossRef]
67. Jiang, J.; Shi, D.; Niu, S.; Liu, S.; Liu, Y.; Zhao, B.; Zhang, Y.; Liu, H.; Zhao, Z.; Li, M.; et al. Modulating electron density enable efficient cascade conversion from peroxymonosulfate to superoxide radical driven by electron-rich/poor dual sites. *J. Hazard. Mater.* **2024**, *468*, 133749. [CrossRef]

68. Ren, Q.; Liu, J.; Yang, Z.; Yang, Q. Boosting transformation of dissolved oxygen to superoxide radical: Function of P25. *Water Environ. Res.* **2023**, *95*, e10898. [CrossRef]
69. Zhang, C.; Deng, Y.; Wan, Q.; Zeng, H.; Wang, H.; Yu, H.; Pang, H.; Zhang, W.; Yuan, X.; Huang, J. Built-in electric field boosted exciton dissociation in sulfur doped BiOCl with abundant oxygen vacancies for transforming the pathway of molecular oxygen activation. *Appl. Catal. B Environ.* **2024**, *343*, 123557. [CrossRef]
70. Chen, Y.; Wang, X.; Liu, B.; Zhang, Y.; Zhao, Y.; Wang, S. Directional regulation of reactive oxygen species in titanium dioxide boosting the photocatalytic degradation performance of azo dyes. *J. Colloid Interface Sci.* **2024**, *673*, 275–283. [CrossRef]
71. Yao, Z.; Wang, Q.; Fan, J.; Yu, T.; Zhang, C.; Zhou, X. Efficient decontamination and detoxification of phenols by photocatalytic CQDs@Ag_3PO_4: Re-insights into the targeted reduction and coupling processes of $\cdot O_2^-$ and $^1O_2$. *Sep. Purif. Technol.* **2025**, *353*, 128306. [CrossRef]
72. Xu, X.; Wang, J.; Chen, T.; Yang, N.; Wang, S.; Ding, X.; Chen, H. Deep insight into ROS mediated direct and hydroxylated dichlorination process for efficient photocatalytic sodium pentachlorophenate mineralization. *Appl. Catal. B Environ.* **2021**, *296*, 120352. [CrossRef]
73. Zhang, Y.; Chen, Q.; Qin, H.; Huang, J.; Yu, Y. Identification of Reactive Oxygen Species and Mechanism on Visible Light-Induced Photosensitized Degradation of Oxytetracycline. *Int. J. Environ. Res. Public Health* **2022**, *19*, 15550. [CrossRef] [PubMed]
74. Zhou, L.; Lei, J.; Wang, F.; Wang, L.; Hoffmann, M.R.; Liu, Y.; In, S.-I.; Zhang, J. Carbon nitride nanotubes with in situ grafted hydroxyl groups for highly efficient spontaneous H_2O_2 production. *Appl. Catal. B Environ.* **2021**, *288*, 119993. [CrossRef]
75. Li, Y.F.; Selloni, A. Theoretical study of interfacial electron transfer from reduced anatase TiO_2(101) to adsorbed O_2. *J. Am. Chem. Soc.* **2013**, *135*, 9195–9199. [CrossRef] [PubMed]
76. Khan, Z.U.H.; Gul, N.S.; Sabahat, S.; Sun, J.; Tahir, K.; Shah, N.S.; Muhammad, N.; Rahim, A.; Imran, M.; Iqbal, J.; et al. Removal of organic pollutants through hydroxyl radical-based advanced oxidation processes. *Ecotoxicol. Environ. Saf.* **2023**, *267*, 115564. [CrossRef]
77. Pavel, M.; Anastasescu, C.; State, R.N.; Vasile, A.; Papa, F.; Balint, I. Photocatalytic Degradation of Organic and Inorganic Pollutants to Harmless End Products: Assessment of Practical Application Potential for Water and Air Cleaning. *Catalysts* **2023**, *13*, 380. [CrossRef]
78. Kjellsson, L.; Nanda, K.D.; Rubensson, J.E.; Doumy, G.; Southworth, S.H.; Ho, P.J.; March, A.M.; Al Haddad, A.; Kumagai, Y.; Tu, M.F.; et al. Resonant Inelastic X-Ray Scattering Reveals Hidden Local Transitions of the Aqueous OH Radical. *Phys. Rev. Lett.* **2020**, *124*, 236001. [CrossRef]
79. Berbille, A.; Li, X.F.; Su, Y.; Li, S.; Zhao, X.; Zhu, L.; Wang, Z.L. Mechanism for Generating H_2O_2 at Water-Solid Interface by Contact-Electrification. *Adv. Mater.* **2023**, *35*, 2304387. [CrossRef]
80. Krumova, K.; Cosa, G. Chapter 1. Overview of Reactive Oxygen Species. In *Singlet Oxygen: Applications in Biosciences and Nanosciences*; Royal Society of Chemistry: London, UK, 2016; pp. 1–21.
81. Huang, S.; Xu, Y.; Liu, Q.; Zhou, T.; Zhao, Y.; Jing, L.; Xu, H.; Li, H. Enhancing reactive oxygen species generation and photocatalytic performance via adding oxygen reduction reaction catalysts into the photocatalysts. *Appl. Catal. B Environ.* **2017**, *218*, 174–185. [CrossRef]
82. Liu, C.; Ji, Y.; Shao, Q.; Feng, X.; Lu, X. Thermodynamic analysis for synthesis of advanced materials. *Struct. Bond.* **2009**, *131*, 193–270. [CrossRef]
83. Cheng, B.; Ceriotti, M. Computing the absolute Gibbs free energy in atomistic simulations: Applications to defects in solids. *Phys. Rev. B* **2018**, *97*, 054102. [CrossRef]
84. Tuchagues, J.-P.; Bousseksou, A.; Molnár, G.; McGarvey, J.J.; Varret, F. The Role of Molecular Vibrations in the Spin Crossover Phenomenon. In *Spin Crossover in Transition Metal Compounds III*; Springer: Berlin/Heidelberg, Germany, 2006; pp. 84–103; ISBN 978-3-540-44984-3.
85. Hanh, T.T.T.; Van Hoa, N. Zero-Point Vibration of the Adsorbed Hydrogen on the Pt(110) Surface. *Divers. Quasipart. Prop. Emerg. Mater.* **2022**, 303–315. [CrossRef]
86. Bajpai, A.; Mehta, P.; Frey, K.; Lehmer, A.M.; Schneider, W.F. Benchmark First-Principles Calculations of Adsorbate Free Energies. *ACS Catal.* **2018**, *8*, 1945–1954. [CrossRef]
87. Diesen, V.; Jonsson, M. Formation of H_2O_2 in TiO_2 photocatalysis of oxygenated and deoxygenated aqueous systems: A probe for photocatalytically produced hydroxyl radicals. *J. Phys. Chem. C* **2014**, *118*, 10083–10087. [CrossRef]
88. Friesner, R.A. Ab initio quantum chemistry: Methodology and applications. *Proc. Natl. Acad. Sci. USA* **2005**, *102*, 6648–6653. [CrossRef] [PubMed]
89. Cremer, D. Møller–Plesset perturbation theory: From small molecule methods to methods for thousands of atoms. *Wiley Interdiscip. Rev. Comput. Mol. Sci.* **2011**, *1*, 509–530. [CrossRef]
90. Ayala, P.Y.; Scuseria, G.E. Linear scaling second-order Moller–Plesset theory in the atomic orbital basis for large molecular systems. *J. Chem. Phys.* **1999**, *110*, 3660–3671. [CrossRef]

91. Frisch, M.J.; Trucks, G.W.; Schlegel, H.B.; Scuseria, G.E.; Robb, M.A.; Cheeseman, J.R.; Scalmani, G.; Barone, V.; Petersson, G.A.; Nakatsuji, H.; et al. *Gaussian 16, Revision C.01*; Gaussian, Inc.: Wallingford, CT, USA, 2016.
92. Riley, K.E.; Hobza, P. Assessment of the MP2 method, along with several basis sets, for the computation of interaction energies of biologically relevant hydrogen bonded and dispersion bound complexes. *J. Phys. Chem. A* **2007**, *111*, 8257–8263. [CrossRef]
93. Feyereisen, M.; Fitzgerald, G.; Komornicki, A. Use of approximate integrals in ab initio theory. An application in MP2 energy calculations. *Chem. Phys. Lett.* **1993**, *208*, 359–363. [CrossRef]
94. Zhang, Y.; Dai, M.; Yuan, Z. Methods for the detection of reactive oxygen species. *Anal. Methods* **2018**, *10*, 4625–4638. [CrossRef]
95. Shi, X.; Back, S.; Gill, T.M.; Siahrostami, S.; Zheng, X. Electrochemical Synthesis of H_2O_2 by Two-Electron Water Oxidation Reaction. *Chem* **2021**, *7*, 38–63. [CrossRef]
96. Keller, E.; Tsatsoulis, T.; Reuter, K.; Margraf, J.T. Regularized second-order correlation methods for extended systems. *J. Chem. Phys.* **2022**, *156*, 24106. [CrossRef]
97. Piris, M. Dynamic electron-correlation energy in the natural-orbital-functional second-order-Møller-Plesset method from the orbital-invariant perturbation theory. *Phys. Rev. A* **2018**, *98*, 022504. [CrossRef]
98. Li, X.; Liu, S.; Cao, D.; Mao, R.; Zhao, X. Synergetic activation of H_2O_2 by photo-generated electrons and cathodic Fenton reaction for enhanced self-driven photoelectrocatalytic degradation of organic pollutants. *Appl. Catal. B Environ.* **2018**, *235*, 1–8. [CrossRef]
99. Cao, P.; Quan, X.; Zhao, K.; Chen, S.; Yu, H.; Niu, J. Selective electrochemical H_2O_2 generation and activation on a bifunctional catalyst for heterogeneous electro-Fenton catalysis. *J. Hazard. Mater.* **2020**, *382*, 121102. [CrossRef] [PubMed]
100. Zeng, H.; Zhang, G.; Ji, Q.; Liu, H.; Hua, X.; Xia, H.; Sillanpää, M.; Qu, J. PH-Independent Production of Hydroxyl Radical from Atomic H*-Mediated Electrocatalytic H_2O_2 Reduction: A Green Fenton Process without Byproducts. *Environ. Sci. Technol.* **2020**, *54*, 14725–14731. [CrossRef] [PubMed]
101. MacManus-Spencer, L.A.; McNeill, K. Quantification of singlet oxygen production in the reaction of superoxide with hydrogen peroxide using a selective chemiluminescent probe. *J. Am. Chem. Soc.* **2005**, *127*, 8954–8955. [CrossRef]
102. Schürmann, A.; Luerßen, B.; Mollenhauer, D.; Janek, J.; Schröder, D. Singlet Oxygen in Electrochemical Cells: A Critical Review of Literature and Theory. *Chem. Rev.* **2021**, *121*, 12445–12464. [CrossRef]
103. Dennington, R.; Keith, T.A.; Millam, J.M. *GaussView*, Version 6; Semichem Inc.: Shawnee, KS, USA, 2019.